# Fatigue behaviour of NiTi shape memory alloy scaffolds produced by SLM, a unit cell design comparison

M. Speirs, B. Van Hooreweder, J. Van Humbeeck, J.-P. Kruth

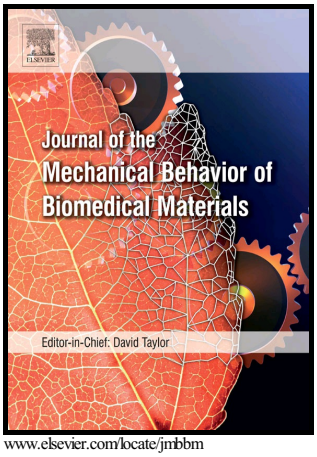


www.elsevier.com/locate/jmbbm

PII: S1751-6161(17)30023-1
DOI: http://dx.doi.org/10.1016/j.jmbbm.2017.01.016
Reference: JMBBM2187

To appear in: *Journal of the Mechanical Behavior of Biomedical Materials*

Received date: 15 October 2016
Revised date: 8 January 2017
Accepted date: 11 January 2017

Cite this article as: M. Speirs, B. Van Hooreweder, J. Van Humbeeck and J.-P. Kruth, Fatigue behaviour of NiTi shape memory alloy scaffolds produced by SLM, a unit cell design comparison, *Journal of the Mechanical Behavior of Biomedical Materials,* http://dx.doi.org/10.1016/j.jmbbm.2017.01.016

# Fatigue behaviour of NiTi shape memory alloy scaffolds produced by SLM, a unit cell design comparison

M. Speirs[1*], B. Van Hooreweder[1], J. Van Humbeeck[2], J.-P. Kruth[1]

[1]*Department of Mechanical Engineering, KU Leuven, Leuven, Belgium*

[2]*Department of Materials Engineering, KU Leuven, Leuven, Belgium*

[*]Corresponding Author. Mathew Speirs, tel: +3216322772, fax: +3216322987. mathew.speirs@kuleuven.be



**Abstract**

Selective laser melting (SLM) is an additive manufacturing technique able to produce complex functional parts via successively melting layers of metal powder. This process grants the freedom to design highly complex scaffold components to allow bone ingrowth and aid mechanical anchorage.

This paper investigates the compression fatigue behaviour of three different unit cells (octahedron, cellular gyroid and sheet gyroid) of SLM nitinol scaffolds. It was found that triply periodic minimal surfaces display superior static mechanical properties in comparison to conventional octahedron beam lattice structures at identical volume fractions. Fatigue resistance was also found to be highly geometry dependent due to the effects of AM processing techniques on the surface topography and notch sensitivity. Geometries minimising nodal points and the staircase effect displayed the greatest fatigue resistance when normalized to yield strength. Furthermore oxygen analysis showed a large oxygen uptake during SLM processing which must be altered to meet ASTM medical grade standards and may significantly reduce fatigue life. These achieved fatigue properties indicate that NiTi scaffolds produced via SLM can provide sufficient mechanical support over an implants lifetime within stress range values experienced in real life.

*Keywords*: Additive manufacturing; Nickel Titanium; Fatigue; Mechanical properties; Selective laser melting

## 1. Introduction

Nitinol (NiTi), a near equiatomic nickel-titanium alloy, is seeing wide use in both medical[1-3] and non-medical applications such as actuators or as couplings and fasteners[4]. This is due to

its unique characteristics of superelasticity and shape memory coupled with biocompatibility, large recoverable strains and corrosion resistance[5]. However one hindrance in this alloys widespread use is its difficulty in manufacturing and processing while maintaining functional properties[6]. To overcome this, additive manufacturing (AM) techniques such as selective laser melting (SLM)[7] have been successfully developed for nitinol[8, 9].

Nitinol parts are often used in demanding applications in both the medical and industrial sector and hence fatigue life assessment is important. Currently, the majority of available data on nitinol fatigue life is based on cyclic loading under uniaxial testing[10]. For biomedical applications superelastic nitinol is more commonly employed due to its superior fatigue resistance and where crack initiation dominates the fatigue behaviour[11]. Other factors affecting fatigue resistance such as impurities, inclusions, grain size and grain orientation can be improved by grain size reduction or reducing impurity content[11]. A method for reducing impurity pickup during SLM processing has been developed for nitinol[12, 13].

Studies on the fatigue properties of porous AM nitinol are currently limited. One study has found that porous nitinol samples at volume fractions >80% were stable at up to stress amplitudes of 1.4 times their yield stress[14]. Fatigue studies on porous titanium have shown that oxygen uptake above 0.35wt% during processing via the space holder technique can produce embrittlement greatly decreasing fatigue life[15]. SLM of Ti6Al4V showed that higher porosity resulted in reduced fatigue life however normalised yield S-N curves were overlapping conforming to the power law[16, 17]. Also surface quality was found as a key factor influencing the fatigue resistance of solid and porous materials and recent work has shown that etching techniques applied to porous AM produced structures significantly improves both quasi-static and cyclic mechanical performance[18, 19]. Additionally, a fatigue comparison between AM and traditional manufacturing processes has shown a superior life for AM components if stress relieved in both AlSi10Mg and Ti6Al4V[20].

Other factors such as unit cell design have been shown to affect fatigue life with unit cells reducing the overall number of nodal points displaying superior fatigue life[21]. Currently the octahedron unit cell is widely used due to its feasibility for SLM as the design contains no overhangs and displays strong anisotropy[22]. However the manufacturing design capabilities currently only seen in AM can be utilised further for fatigue optimisation in the production of complex shapes such as triply periodic surfaces[23]. Triply periodic minimal surfaces (TPMS) may be used for scaffold designs and consist of a sheet like architecture. They have already been shown to be suitable for biomedical applications due to their high specific stiffness to weight ratios while maintaining isotropy[24, 25]. Furthermore a wide library of minimal surfaces are available and other important biological factors such as permeability have been assessed allowing a large degree of design flexibility[26]. Other advantages of TPMS in relation to fatigue life is due to their continuous curvature and sheet like structure, the effect of stress concentrators at nodal points is eliminated. Additionally, at identical volume fractions lattice

like structures will display a larger surface to volume ratio in relation to TPMS structures. Therefore in this study minimal pore size and volume fraction were maintained constant to allow an adequate fatigue behaviour comparison while remaining relevant in relation to in-vitro/vivo responses. Porous NiTi foams have previously shown successful cell proliferation and differentiation with Ni ion release below cytotoxic levels[27].

The aim of this work is hence to investigate the fatigue behaviour of NiTi scaffolds with three different unit cell designs manufactured by selective laser melting. The SLM NiTi alloy samples were characterized for their mechanical properties in both monotonic and cyclic compression loading conditions. Although for orthopaedic implant applications in vivo conditions are highly complex, the present investigation under compression loading conditions provides useful data on the effects of cell design on fatigue behaviour of NiTi produced via SLM.

## 2. Materials and experiments

### 2.1 Materials and manufacturing

For this study, one type of open porous cylindrical scaffold with 15mm height and 10mm diameter was produced with three different unit cell designs namely octahedron, cellular gyroid and sheet gyroid. The geometry and morphological properties of the unit cells are presented in Figure 1 and Table 1 respectively. Two TPMS unit cells were chosen: the gyroid unit cell with a sheet like structure and the cellular gyroid structure where an offset is applied to create a more standard lattice like shape. In conjunction with this, a standard beam lattice using an octahedron unit cell was studied as shown in Figure 1. All parts for this study were designed using Magics software [Materialise NV, Leuven, Belgium]. For both TPMS designs the initial unit cells were generated in K3Dsurf software (http://k3dsurf.sourceforge.net) before being imported into Magics. A total of 15 samples of each design were made. All designs were produced by an in-house developed SLM machine that uses an IPG Yb:YAG fire laser of 300W (spot size 80µm). The basic powder was produced by plasma atomisation with a nominal Ni content of 55.2 Wt% produced by AP & C inc., Raymor, Quebec, Canada. The particle size range used was 25-45µm. Each part was processed with a laser power of 40W, a scanning speed of 160mm/s and a hatch spacing of 75µm[28]. All cylinders were built upright parallel to the build direction on a nitinol baseplate and were removed post production via electrical discharge machining (EDM).

Post production, all samples were solution treated at 1000$^{o}$C for 120 min after sealing in argon quartz tubes followed by water quenching to ensure a fully austenitic structure. Both the initial nitinol powder and one SLM produced sheet gyroid scaffold after solution treatment were sent for instrumental gas analysis (IGA) testing. The amount of oxygen

pickup was assessed via heating above 2500°C in an inert Ar atmosphere with any oxygen release picked up via infrared detectors.

### 2.2 Morphological characterization

The dimensional aspects of the scaffolds morphologies were calculated via dry weighing and micro computed tomography. For dry weighing the volume fraction of the samples was calculated using five randomly selected samples from each unit cell design. Overall porosity was calculated by dividing the actual weight by the theoretical weight of the macro volume using a density of 6.45g/cm$^3$ for NiTi. Archimedes measurements were completed using pure ethanol and an Acculab Atilon ATL-224-I balance (Acculab, Massachusetts, America). Microfocus X-ray computed tomography (Micro-CT)-based morphological characterization of the NiTi scaffolds was performed using a Phoenix NanoTom S (GE Measurement and Control Solutions, Wunstorf, Germany) with a 180kV / 15 W high performance nanofocus X-ray tube and a 2304x2304 pixel Hamamatsu detector. A voltage of 90 kV and a current of 240 µA were applied. A tungsten target was used and a 0.3mm copper filter was installed. Each sample was scanned over 360° with a 0.15° rotation step, an exposure time of 500ms with no image skip and no frame averaging was applied. After scanning reconstruction was completed using Phoenix datos/x 2.0 reconstruction software (GE Measurement and Control Solutions, Wunstorf, Germany). The resulting images had an isotropic voxel size of 6.5 µm. CTAn software (Bruker micro-CT, Kontich, Belgium) was applied for 3D morphological analysis of the µCT data. Automatic Otsu segmentation[29] was applied for binarization of the reconstructed µCT images.

Each scaffold geometry was viewed using scanning electron microscopy (SEM; Phillips, XL 30, Germany) operating at 10kV. An ultrasonic cleaning in ethanol solution for 10 minutes was completed before analysis. The volume fraction and beam thickness were calculated for each design with the structure thickness calculated in 3D using a sphere fitting algorithm[30]. The transformation behaviour was studied by differential scanning calorimetry (DSC) using a TA Q2000 calorimeter (TA instruments, Delaware, America) with a cooling/heating rate of 10Kmin$^{-1}$ in a helium gas atmosphere. To minimize errors of the sample temperature measurements, the samples were attached to a PT-100 sensor, which was used to control the temperature scans. Both octahedron and sheet gyroid solution treated samples were assessed from -150$^o$C to +150$^o$C.

### 2.3 Mechanical testing

Static mechanical testing was completed using an Instron Electropuls (Instron, Massachusetts, America) E10.000 with a 10kN force cell. All quasi static tests were completed by applying a constant deformation rate of 0.2mm/min. All samples were tested to ISO13314:2011 with zinc stearate used as a lubricant. This standard was used to calculate both the plateau stress ($\sigma_{pl}$) and the yield stress ($\sigma_y$). For fatigue testing all samples underwent testing at constant amplitude sinusoidal loading in compression-compression at

fixed test frequency of 15Hz and fixed load ratio R=0.1. All experiments were force controlled and the stress based approach was used for fatigue analysis. SN-curves were constructed by testing two identical samples at every stress amplitude for each unit cell design. Maximum stress values were determined at fixed percentages (20% - 90%) of the measured plateau stress. The failure criteria were defined as the moment where the test reached $1x10^7$ cycles (run out), or when a sudden decrease in displacement occurred (1mm/s). All tests were completed at $20^oC$. During every test, the load, displacement and temperature were monitored. A compliance correction was applied to account for the deflection of the load frame. To allow lateral expansion of the samples during loading in compression, zinc stearate was placed between the sample and the hardened compression plates. In line with all previous works on fatigue of scaffolds, SN-curves were first constructed by plotting the global maximum stress as function of the cycles to failure. In a next step, these global stress values were normalized with the yield stress.



**3. Results**

The Micro-CT and dry weighing results show a large increase in volume fraction in comparison to designed values as shown in Table 2. This can be attributed to the partially sintered particles picked up during SLM production. This is further corroborated by the increase in surface area. Static mechanical testing of the three different unit cell designs showed the plateau stress varied between 27-78MPa as shown in Table 2. The micro-architectures therefore have a large effect on the static mechanical properties. The octahedron unit cell displayed the lowest yield and plateau stress with the sheet gyroid displaying the highest.

Figure 2 shows the DSC curves of the solution treated samples for both sheet gyroid and Octahedron. Due to the similarity in both cellular gyroid and octahedron DSC graphs owing to their lattice like structure only Octahedron and sheet gyroid are shown. For both cases, broad peaks are observed indicating phase segregation or impurity pickup during processing which can be due to oxygen pickup. More details on oxygen pickup during SLM of nitinol can be found in[12, 13]. From the IGA analysis the non-virgin base powder used was shown to contain an O content of 430ppm. However post production and solution treatment a value of 720ppm was found. This value does not meet the required standard ASTM F2603-05

where values of <500ppm must be achieved. Both curves display similar transformation criteria suggesting a mainly austenitic phase at room temperature and no microstructure variation between scaffold design.

Fatigue testing showed vastly different results between each unit cell design if absolute stress values are considered as indicated in Figure 3a. It can be seen that even when the fatigue life of the three structures is normalized with respect to their plateau stress (Figure 3b) a difference in fatigue life is observed. The $R^2$ values for each design showed an extremely high correlation ranging from 0.97-0.99. The normalized S-N curves show that the sheet gyroid clearly outperforms both the cellular gyroid and octahedron designs.

The permanent deformation vs number of cycles is presented in Figure 4. It can be seen that the typical three stage behaviour of porous metal is not observed[31]. Stage I normally involves small strain accumulation over the initial few cycles and cannot be clearly seen for all three designs. Stage II is identified as a period of minimal strain accumulation with the octahedron unit cell displaying the lowest amount of strain accumulation over stage II in relation to both gyroid designs. Stage III highlights the point of rapid strain accumulation until each sample was found to fail in shear at 45° defining the samples fatigue life. From here it can be seen for the octahedron samples display a far lower amount of strain accumulation occurs until sudden complete failure.

The SEM images of failed samples at both the lowest and highest stress values used for each design are shown in Figure 6. All samples were found to fail in 45 degree shear as shown in Figure 5. It can be seen that at lower stress levels multiple crack initiation sites are found for both lattice structures and are indicated with arrows. It can be noted that for both lattice structures cellular gyroid and octahedron crack initiation to failure has occurred at the nodal points. At low stresses no clear crack initiation point can be observed within the sheet gyroid sample. The produced structures were uniform in architecture with a slight increase in designed volume fraction due to residual particle pickup as seen in Table 2 and Figure 6. Additionally a very small amount of internal porosity was seen within each design as shown in Table 2.



**4. Discussion**

It has been shown that both quasi-static and dynamic mechanical performance is highly dependent on unit cell design with TPMS structures displaying superior fatigue life in relation to octahedron scaffold unit cells. The quasi-static mechanical properties for all 3 unit cell designs are shown to be within the range of mechanical properties of cortical and trabecular bone[32]. It was found that sheet gyroid displayed the most superior fatigue life

even when normalised in relation to their plateau stress properties. Normalized S-N curves are shown to also display superior fatigue properties for both TPMS unit cells with all three displaying extremely high coefficients of determination $R^2$ >0.97 and with sheet gyroid displaying the highest fatigue life. The possibilities for their superior fatigue life are potentially due to the following reasons. Both TPMS structures alter at a continuous rate of curvature. This firstly helps to minimize the staircase effect inherent to AM processing techniques which could potentially enhance crack initiation. Secondly, residual particles which are located on down facing surfaces may act as stress concentrators throughout the scaffold allowing crack initiation. For the octahedron unit cell, due to its lattice like design, a greater surface area is in contact with the powder bed during processing, as shown in Table 1. This results in a greater amount of residual particles attached overall as can be seen in Figure 6. This can be further visualized with Figure 7 which highlights the possible increase in notch sensitivity due to residule particle pickup in the octahedron unit cell design. However due to the initial constraints in terms of identical pore size and volume fraction provided to allow an accurate comparison and be relative to bio-applications (equal pore size and volume fraction) the cellular gyroid design consisted of much thicker struts resulting in the lowest surface area of the three designs.

At cyclic stress values below 0.3 $\sigma_y$, samples in both gyroid unit cell designs were able to achieve above $10^6$ loading cycles, which is similar to other normalized stress values of lattice unit cells tested in Ti6Al4V (ELI)[21]. However, one must consider the effect of surface topography and unit cell design as different designs were used and etching techniques must be considered to further improve fatigue life [33]. Furthermore in relation to their normalized S-N curves it is important to understand what is causing the improved fatigue life for the sheet gyroid unit cell. Analysis of the fracture surfaces under SEM showed a difference between the unit cells loaded under high and low stress amplitudes (Figure 6). It can be seen that at low stress amplitudes multiple crack initiation sites are observed for both TPMS structures. Furthermore it can be clearly seen that both those structures due to their continuous rate of curvature contain no clear notch points which can act as stress concentrators.

Both the IGA and DSC results indicate a significant impurity pickup during processing. This can be highlighted by the amount of oxygen pickup resulting in the final component not adhering to medical grade nitinol requirements ASTM F2063-05. However it can be seen that the initial powder oxygen content is already near the limit of 420ppm. Therefore as well as minimizing impurity pickup during SLM via flushing techniques[12], other atomisation techniques[34] or blending[35] could be applied to start with a more virgin powder. It must also be noted that the initial SLM powder had been reused multiple times before this production run which could additionally apply to the high powder O content. Therefore it is recommended to regularly reassess your powders O content over time to check if still viable for medical grade production. Furthermore impurity pickup will further reduce fatigue life through embrittlement and inclusion initiation sites as well as potentially changing the

failure mechanism[36].

An improved fatigue life is important for non reabsorbable metallic porous orthopaedic implants. Through improved fatigue life a lower volume fraction of implant material can be used which can be beneficial in terms of implant longevity as implant removal for porous structures is not an option in most cases .

Another advantage of nitinol is its ability to more closely mimic mechanical loading in relation to bone when compared to other potential allows and this is shown to stimulate osteoconductivity. In this case NiTi, while in the austenite phase, is advantageous over other titanium based alloys[11].

## 5. Conclusions

The fatigue behaviour of different NiTi unit cell designs produced via selective laser melting was studied in this paper. Three types of unit cell were investigated, namely the octahedron, cellular gyroid and sheet gyroid. It was found that the quasi-static compression properties found were within the range of cortical and trabecular bone for all three unit cell designs. The absolute S-N curves were found to be higher for both triply periodic unit cell designs. The normalized S-N curves further show a difference in unit cell design with again the triply periodic unit cells displaying a superior fatigue resistance in relation to the octahedron unit cell. This superior fatigue resistance can be attributed to the removal of nodal points which may act as stress concentrators for crack initiation. Furthermore, other detrimental effects inherent to AM processing such as residual particle attachment and the staircase effect are minimised via TPMS designs. This defect tolerant design can be further applied to other triply periodic minimal surfaces and other AM production methods and their respective fatigue behaviour assessed.



## Acknowledgements

The authors acknowledge support within the EU 7th framework program (FP7) under Marie Curie ITN project BioTiNet (grant No. 264635) and support from the FWO (Fonds wetenschappelijk Onderzoek) Vlaanderen (grant No. 12S4615N). The assistance of D.Winant with the DSC measurements and J.Umans with figure processing is also highly appreciated.

## References

1. T. Duerig, A. Pelton, D. Stöckel, *Materials Science and Engineering: A* **273–275** 149 (1999).
2. N.S. Moghaddam, R. Skoracki, M. Miller, M. Elahinia, D. Dean, *Procedia CIRP* **49** 45 (2016).
3. N.B. Morgan, *Materials Science and Engineering: A* **378** 16 (2004).
4. J. Van Humbeeck, *Materials Science and Engineering: A* **273–275** 134 (1999).
5. S. Dadbakhsh, M. Speirs, J. Van Humbeeck, J.-P. Kruth, *MRS Bulletin* **41** 765 (2016).

6. M.H. Elahinia, M. Hashemi, M. Tabesh, S.B. Bhaduri, *Progress in Materials Science* **57** 911 (2012).
7. J.P. Kruth, G. Levy, F. Klocke, T.H.C. Childs, *CIRP Annals - Manufacturing Technology* **56** 730 (2007).
8. T. Bormann, B. Müller, M. Schinhammer, A. Kessler, P. Thalmann, M. de Wild, *Materials Characterization* **94** 189 (2014).
9. S. Dadbakhsh, M. Speirs, J.-P. Kruth, J. Schrooten, J. Luyten, J. Van Humbeeck, *Advanced Engineering Materials* **16** 1140 (2014).
10. S.W. Robertson, A.R. Pelton, R.O. Ritchie, *International Materials Reviews* **57** 1 (2012).
11. M.J. Mahtabi, N. Shamsaei, M.R. Mitchell, *Journal of the Mechanical Behavior of Biomedical Materials* **50** 228 (2015).
12. H. Christoph, E. Mohammad, M.W. Jason, M. Horst, F. Jan, *Smart Materials and Structures* **23** 104002 (2014).
13. M. Speirs, X. Wang, S. Van Baelen, A. Ahadi, S. Dadbakhsh, J.-P. Kruth, et al., *Shape Memory and Superelasticity* **2** 310 (2016).
14. S. Bernard, V. Krishna Balla, S. Bose, A. Bandyopadhyay, *Journal of the Mechanical Behavior of Biomedical Materials* **13** 62 (2012).
15. S. Özbilen, D. Liebert, T. Beck, M. Bram, *Materials Science and Engineering: C* **60** 446 (2016).
16. S. Amin Yavari, R. Wauthle, J. van der Stok, A.C. Riemslag, M. Janssen, M. Mulier, et al., *Materials Science and Engineering: C* **33** 4849 (2013).
17. F. Li, J. Li, H. Kou, L. Zhou, *Materials Science and Engineering: C* **60** 485 (2016).
18. G. Pyka, G. Kerckhofs, I. Papantoniou, M. Speirs, J. Schrooten, M. Wevers, *Materials* **6** 4737 (2013).
19. B. Van Hooreweder, Y. Apers, K. Lietaert, J.-P. Kruth, *Acta Biomaterialia*.
20. S. Beretta, S. Romano, *International Journal of Fatigue*.
21. S. Amin Yavari, S.M. Ahmadi, R. Wauthle, B. Pouran, J. Schrooten, H. Weinans, et al., *Journal of the Mechanical Behavior of Biomedical Materials* **43** 91 (2015).
22. S.M. Ahmadi, G. Campoli, S. Amin Yavari, B. Sajadi, R. Wauthle, J. Schrooten, et al., *Journal of the Mechanical Behavior of Biomedical Materials* **34** 106 (2014).
23. D.J. Yoo, *Biomaterials* **32** 7741 (2011).
24. V.J. Challis, X. Xu, L.C. Zhang, A.P. Roberts, J.F. Grotowski, T.B. Sercombe, *Materials & Design* **63** 783 (2014).
25. A. Yánez, A. Herrera, O. Martel, D. Monopoli, H. Afonso, *Materials Science and Engineering: C* **68** 445 (2016).
26. S.C. Kapfer, S.T. Hyde, K. Mecke, C.H. Arns, G.E. Schröder-Turk, *Biomaterials* **32** 6875 (2011).
27. I. Gotman, D. Ben-David, R.E. Unger, T. Böse, E.Y. Gutmanas, C.J. Kirkpatrick, *Acta Biomaterialia* **9** 8440 (2013).
28. M. Speirs, S. Buls, J. Schrooten, J. Luyten, J. Van Humbeeck, J.P. Kruth, in VRAP Advanced Research in Virtual and Rapid Prototyping (Taylor and Francis, Leiria, 2013).
29. T. Kurita, N. Otsu, N. Abdelmalek, *Pattern Recognition* **25** 1231 (1992).
30. (2016).
31. Y. Sugimura, A. Rabiei, A.G. Evans, A.M. Harte, N.A. Fleck, *Materials Science and Engineering: A* **269** 38 (1999).
32. J.-Y. Rho, L. Kuhn-Spearing, P. Zioupos, *Medical Engineering & Physics* **20** 92 (1998).
33. G. Pyka, A. Burakowski, G. Kerckhofs, M. Moesen, S. Van Bael, J. Schrooten, et al., *Advanced Engineering Materials* **14** 363 (2012).
34. G. Schulz, (Google Patents2002).
35. I. Shishkovsky, I. Yadroitsev, I. Smurov, *Physics Procedia* **39** 447 (2012).
36. J. Mentz, M. Bram, H.P. Buchkremer, D. Stöver, *Advanced Engineering Materials* **8** 247 (2006).

Table 1: Overview of each unit cell designed and tested in this current study and their designed geometrical properties given from the CAD designs.

| | | Strut thickness (µm) | Pore size (µm) | Surface area ($cm^2$) | volume fraction (%) | Unit cell size (mm) |
|---|---|---|---|---|---|---|
| Designed values | Octahedron | 260 | 1000 | 36.7 | 20.7 | 1.75 |
| | Cellular gyroid | 320 | 850 | 21.9 | 21.6 | 1.65 |
| | Sheet gyroid | 195 | 900 | 29.3 | 21.5 | 1.4 |

Table 2: Overview of each unit cell measured morphological properties from micro-CT and mechanical testing.

| | | Micro-CT | | | | Mechanical testing | | |
|---|---|---|---|---|---|---|---|---|
| | | Strut thickness (µm) | Internal porosity (%) | Surface area ($cm^2$) | Volume fraction (%) | Dry weighing volume fraction (%) | Yield stress (MPa) | Plateau stress (MPa) |
| Experimental values | Octahedron | 248 | 0.10 | 41.1 | 25.2 | 25.6±0.3 | 21 | 27 |
| | Cellular gyroid | 298 | 0.59 | 26.9 | 25.2 | 24.8±0.4 | 29 | 50 |
| | Sheet gyroid | 210 | 0.07 | 37.2 | 26.6 | 26.9±0.2 | 44 | 78 |



Figure 1: CAD images of each designed unit cell and their respective as produced components: A) Octahedron (Oc), B) Cellular gyroid (CG), C) Sheet gyroid (SG)

Figure 2: DSC curves of solution treated sheet gyroid and octahedron NiTi scaffolds showing the temperatures of martensitic transformations. $M_s$, $M_p$, and $M_f$ demonstrate the martensite transformations upon cooling and $A_s$, $A_p$ and $A_f$ represent all austenite transformations during the heating cycle.

Figure 3: Absolute (A) and normalized, (B) S-N curves for each scaffold geometry.

Figure 4:Accumulated strain vs number of cycles at each stress case and in relation to their yield stress for each unit cell design: A) Octahedron; B) Cellular gyroid; C) Sheet gyroid.

Figure 5: the appearance of tested samples at 0.4 plateau stress at fracture. A) Octahedron; B) Cellular gyroid; C) Sheet gyroid.

Figure 6: SEM micrograph showing the fracture surface at the highest and lowest stress amplitudes tested for each respective design. High stress amplitudes left column and low stress amplitudes right column for each design A) Octahedron; B) Cellular gyroid; C) Sheet gyroid.

Figure 7: A representative visual illustration taken from each CAD design as a 2mm cross section highlighting the amount of residual particles which can potentially attach due to the amount of down facing surfaces. A) Octahedron; B) Cellular gyroid; C) Sheet gyroid.

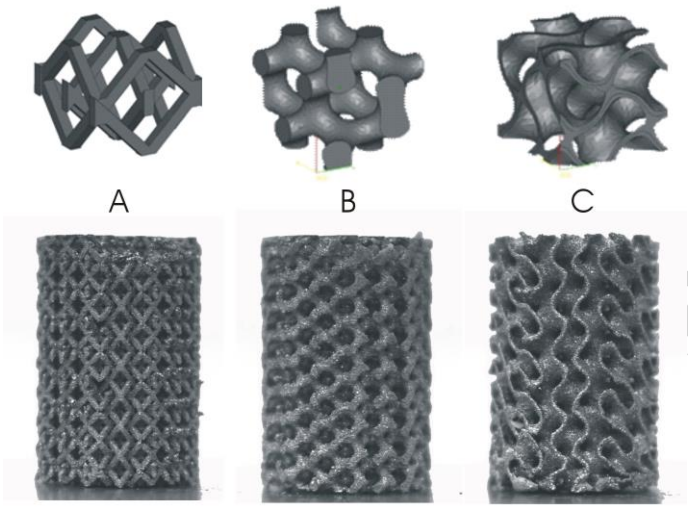

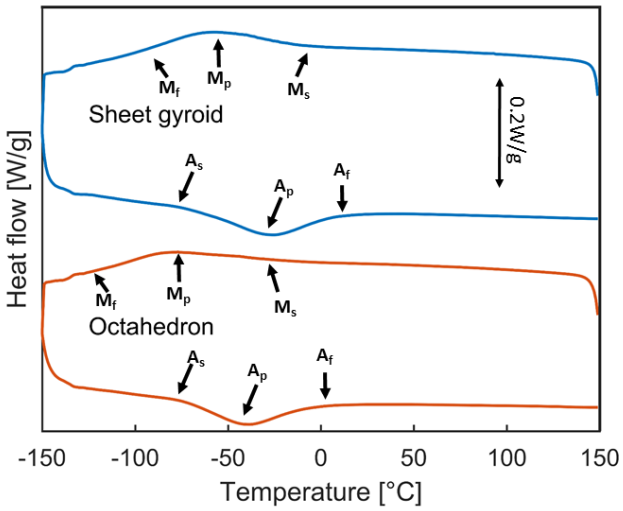

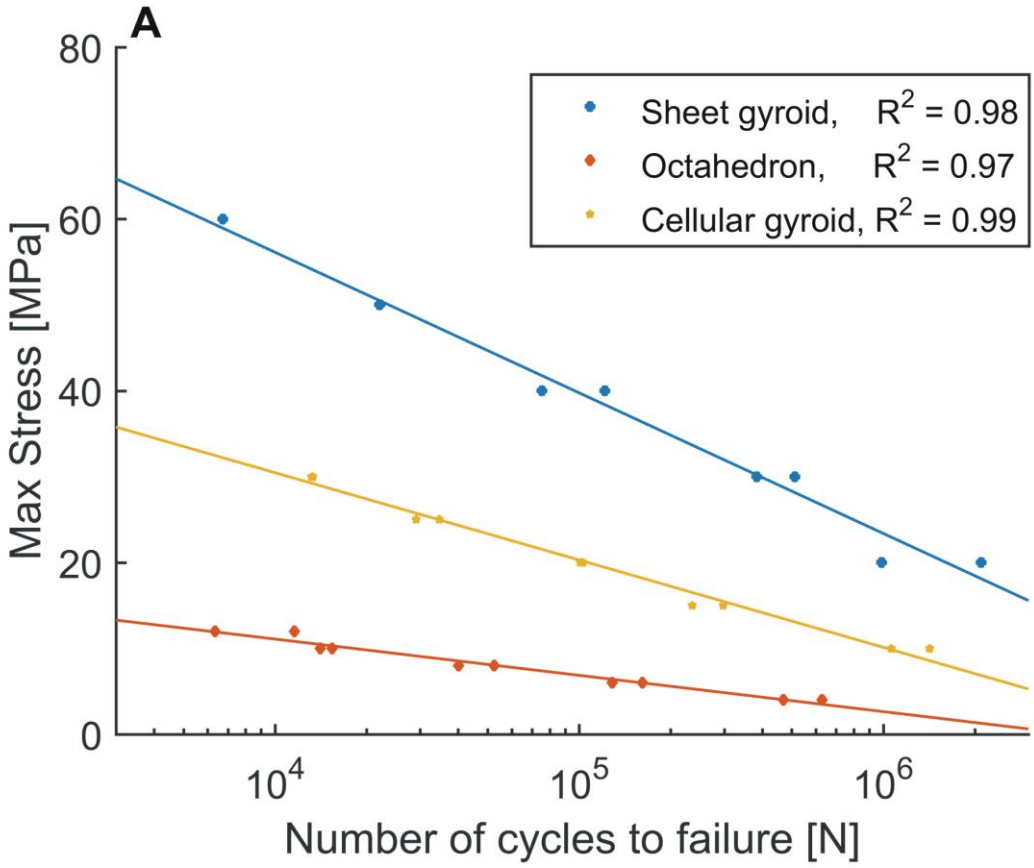
A
80
60
40
20
0
Max Stress [MPa]
Sheet gyroid, R2 = 0.98
Octahedron, R2 = 0.97
Cellular gyroid, R2 = 0.99
10^4
10^5
10^6
Number of cycles to failure [N]

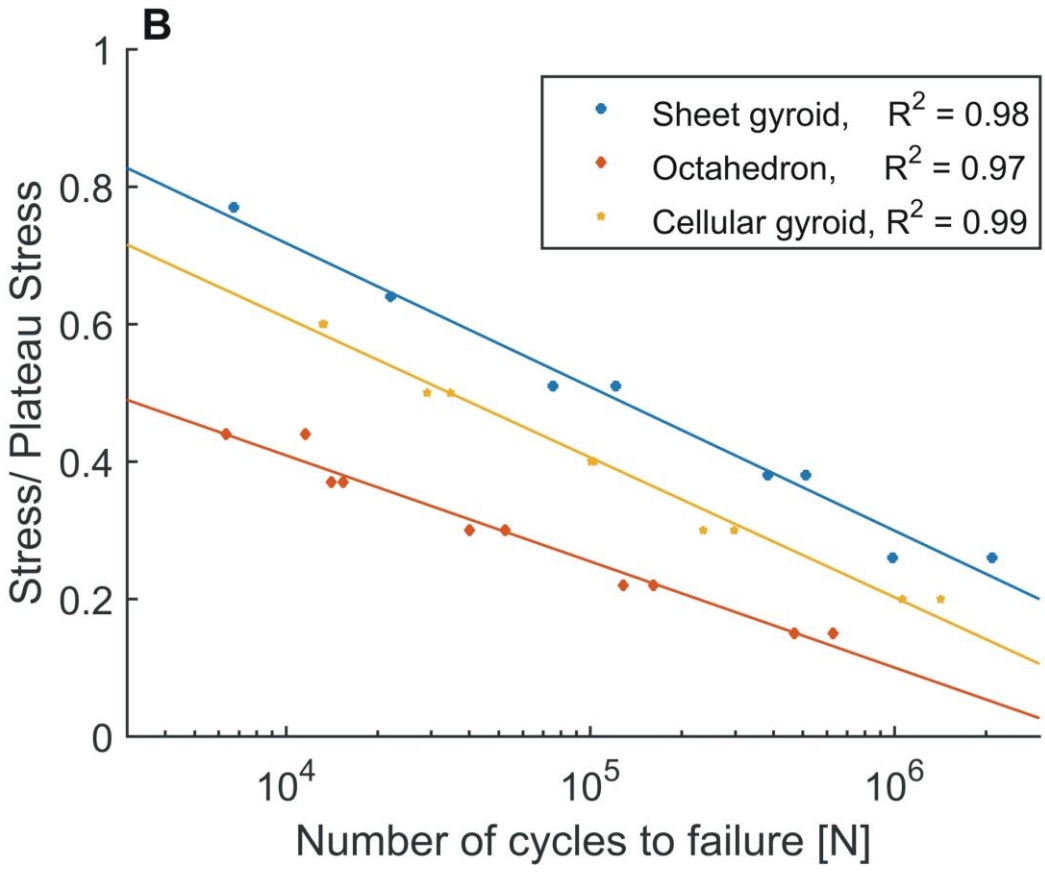
B
1
0.8
0.6
0.4
0.2
0
Stress/ Plateau Stress
Sheet gyroid, R2 = 0.98
Octahedron, R2 = 0.97
Cellular gyroid, R2 = 0.99
10^4
10^5
10^6
Number of cycles to failure [N]

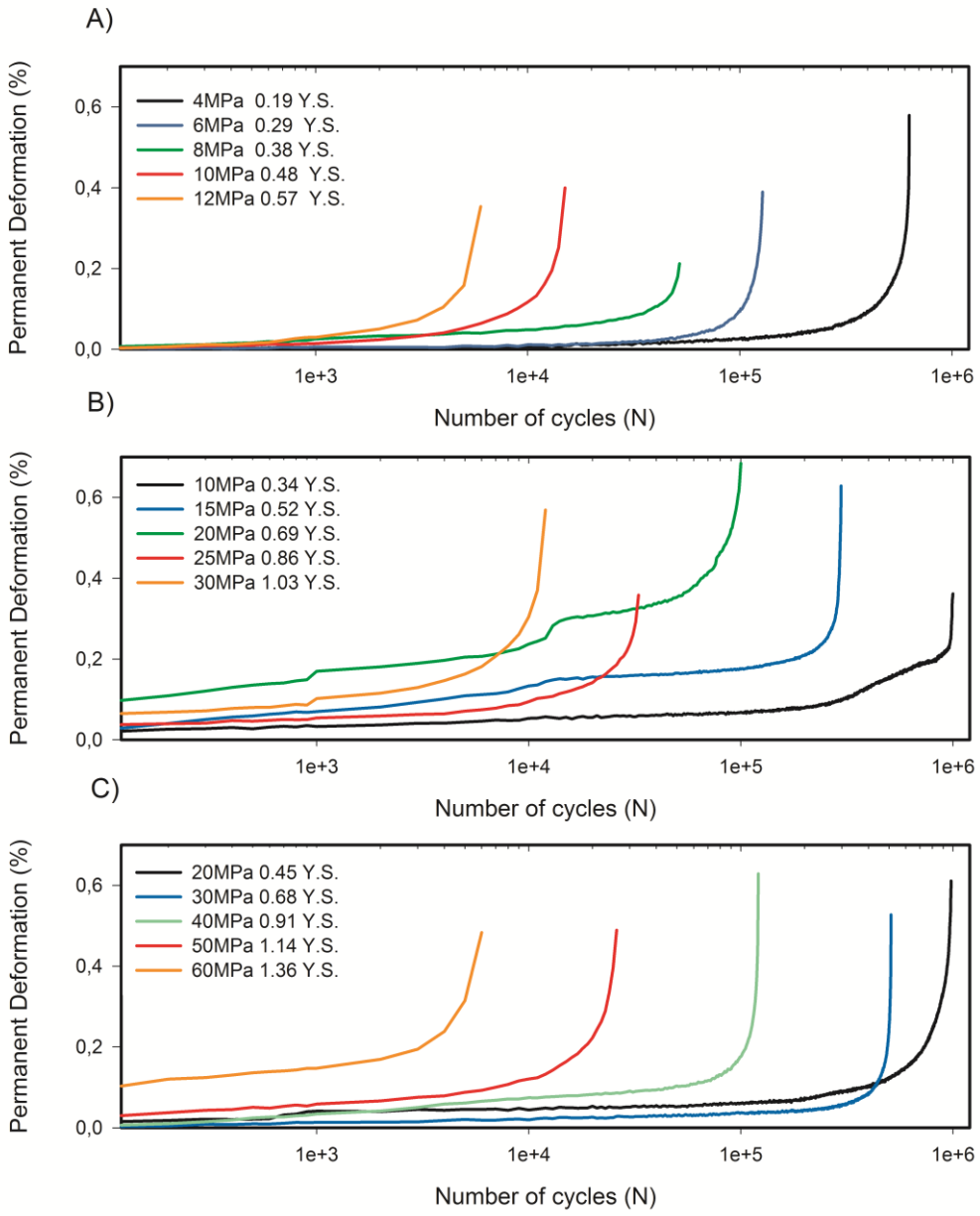
A)
Permanent Deformation (%)
0,0
0,2
0,4
0,6
4MPa 0.19 Y.S.
6MPa 0.29 Y.S.
8MPa 0.38 Y.S.
10MPa 0.48 Y.S.
12MPa 0.57 Y.S.
1e+3
1e+4
1e+5
1e+6
Number of cycles (N)
B)
Permanent Deformation (%)
0,0
0,2
0,4
0,6
10MPa 0.34 Y.S.
15MPa 0.52 Y.S.
20MPa 0.69 Y.S.
25MPa 0.86 Y.S.
30MPa 1.03 Y.S.
1e+3
1e+4
1e+5
1e+6
Number of cycles (N)
C)
Permanent Deformation (%)
0,0
0,2
0,4
0,6
20MPa 0.45 Y.S.
30MPa 0.68 Y.S.
40MPa 0.91 Y.S.
50MPa 1.14 Y.S.
60MPa 1.36 Y.S.
1e+3
1e+4
1e+5
1e+6
Number of cycles (N)